

Signatures of coupling between spin waves and Dirac fermions in YbMnBi_2

A. Sapkota,^{1,*} L. Classen,^{1,2,†} M. B. Stone,³ A. T. Savici,³ V. O. Garlea,³
Aifeng Wang,^{1,‡} J. M. Tranquada,¹ C. Petrovic,¹ and I. A. Zaliznyak^{1,§}

¹*Condensed Matter Physics and Materials Science Division,
Brookhaven National Laboratory, Upton, NY 11973, USA*

²*School of Physics and Astronomy, University of Minnesota, Minneapolis, MN 55415, USA*

³*Neutron Scattering Division, Oak Ridge National Laboratory, Oak Ridge, TN 37831, USA*

(Dated: July 21, 2022)

We present inelastic neutron scattering (INS) measurements of magnetic excitations in YbMnBi_2 , which reveal features consistent with a direct coupling of magnetic excitations to Dirac fermions. In contrast with the large broadening of magnetic spectra observed in antiferromagnetic metals such as the iron pnictides, here the spin waves exhibit a small but resolvable intrinsic width, consistent with our theoretical analysis. The subtle manifestation of spin-fermion coupling is a consequence of the Dirac nature of the conduction electrons, including the vanishing density of states near the Dirac points. Accounting for the Dirac fermion dispersion specific to YbMnBi_2 leads to particular signatures, such as the nearly wave-vector independent damping observed in the experiment.

Dirac and Weyl materials exhibit many exotic and novel quantum phenomena that are both of fundamental and potential technological interest [1–4]. This class of materials encompasses a wide range of condensed matter systems including graphene, d -wave superconductors, and topological insulators and semimetals [1]. The name is derived from their low-energy electronic dispersions that can be described by a relativistic Dirac or Weyl Hamiltonian. The linear variation of energy as a function of wave vector about a Dirac node is a universal feature that leads to novel behaviors such as suppression of backscattering, high carrier mobility, impurity-induced resonant states, spin-polarized transport, and the unusual quantum Hall effect [1–6]. Furthermore, interaction of these low-energy Dirac/Weyl fermions with other degrees of freedom leads to novel physics with technological potential [2, 7, 8]. Hence, understanding coupling of Dirac fermions with other quantum excitations, such as spin waves, is a topic of great current interest.

From this perspective, 112 ternary bismuthides (R, A) MnBi_2 (R = Rare-earth, A = Alkaline-earth: Ca, Sr) represent a particularly interesting family where both magnetism and Dirac fermions coexist, providing a platform to study their interplay [3, 4, 9–11]. In these materials, the Dirac bands and the magnetic order are associated with distinct square-net layers: conducting Bi layers and magnetic MnBi layers separated by layers of R, A , as shown in Fig. 1(a) of Ref. 12. While indirect experimental evidence of a coupling between conduction electrons and magnetic Mn ions is provided by the impact of the magnetic order on electrical transport in CaMnBi_2 [11], inelastic neutron scattering measurements on Sr/ CaMnBi_2 detect no decay of spin waves into particle-hole excitations that would substantiate the coupling [13]. The spin waves appear undamped, no different from the case of an insulator, CaMn_2Sb_2 [14].

RMnBi_2 systems were suggested as possible candidates where coupling of Dirac fermions with spins could be

significant. EuMnBi_2 and YbMnBi_2 are two such recently discovered materials [12]. YbMnBi_2 is particularly interesting because of its possible link with type-II Weyl physics with broken time-reversal symmetry [15–17]. In addition, it holds promise because the ferromagnetic stacking of Mn moments along the c -axis, similar to CaMnBi_2 , suggests that an interlayer exchange interaction can be mediated by Dirac bands [11, 13]. However, the question remains, is there any signature of coupling/entanglement with Dirac fermions in the magnetic excitation spectrum of YbMnBi_2 ? If the coupling does exist, what is the magnitude of this coupling and will magnetic excitations exhibit anomalous broadening, as found in other metallic magnets [13, 18]?

Here, we present the results of INS measurements performed on YbMnBi_2 at 4 different temperatures, spanning the Néel temperature, T_N . We show that the magnetic excitations are well-defined spin waves below T_N , becoming dispersive paramagnons (similar to spin waves) just above T_N , and both can be described with a local-moment Heisenberg model. From our analysis, we extract a damping parameter associated with the observed broadening of the magnetic excitations and compare it to that of both metallic and insulating antiferromagnets. We find that the damping is consistent with the decay of magnetic excitations into Dirac particle-hole pairs and is very different from that usually found in metallic antiferromagnets, such as iron pnictides [18–23]. Unlike electrons in conventional itinerant magnets, the Dirac fermions are stable against antiferromagnetic fluctuations due to their vanishing density of states near the Dirac points, which suppresses the effects of spin-fermion interactions. In addition, Dirac fermions and spin waves in YbMnBi_2 are spatially separated degrees of freedom that primarily propagate in different layers, which further inhibits the coupling. Nevertheless, we show that the damping measured in our INS experiment is consistent with a simple spin-fermion coupling model, which

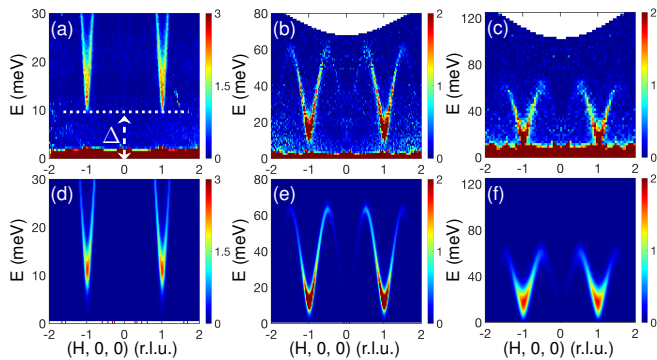


FIG. 1. Spin waves in YbMnBi₂ in the antiferromagnetic state. (a)–(c) INS spectra showing dispersion along $(H, 0, 0)$ direction measured at $T = 4$ K with incident energies $E_i = 35, 100$ and 200 meV, respectively. Dashed line in (a) indicates the spin gap, Δ (cf Table I and Fig. S6). (d)–(f) INS spectra calculated using spin wave dispersion and Eq. (1), with the best fit parameters listed in Table I. For fitting, only the data measured with $E_i = 100$ meV shown in Fig. 2 were used [24]. Intensity scales shown in the colorbars are in arbitrary units and absolute magnitude differs among different E_i .

accounts for the specifics of Dirac dispersion in YbMnBi₂ [16], in the framework of the random phase approximation (RPA). From our experimental results, we determine the coupling constant in this model, which is directly proportional to the experimental damping parameter.

Single crystals of YbMnBi₂ were grown from Bi flux as described in Ref. 12. YbMnBi₂ orders antiferromagnetically below $T_N \approx 290$ K, with an ordered moment of $4.3\mu_B$ at 4 K [12, 25, 26]. INS measurements were performed at SEQUOIA (Figs. 1–3) and HYSPEC [24] spectrometers at the Spallation Neutron Source, Oak Ridge National Laboratory. Four single crystals with the total mass of ≈ 1.8 g were co-aligned in the $(H, 0, L)$ horizontal scattering plane, with the effective mosaic spread of $\lesssim 0.8^\circ$ full-width at half-maximum (FWHM). The measurements were carried out with incident energies $E_i = 35, 100$ and 200 meV at $T = 4, 150, 270$ and 320 K by rotating the sample about its vertical axis in 1° steps over a 270° range (70° for 150 K). Throughout the paper, we index momentum transfer, $\mathbf{Q} = (H, K, L)$ in reciprocal lattice units (rlu) of the $P4/nmm$ lattice, $a = b = 4.48$ Å, $c = 10.8$ Å [12].

Figure 1 (a)–(c) present inelastic neutron scattering spectra for YbMnBi₂ in the antiferromagnetic (AFM) phase at $T = 4$ K, which probe the spin wave dispersion along $(H, 0, 0)$ symmetry direction. Magnetic excitations are well-defined and sharp in both \mathbf{Q} and E , indicating the presence of conventional spin-waves consistent with the local-moment description. The spin waves originate from $\mathbf{Q}_{\text{AFM}} = (\pm 1, 0, 0)$, as expected for a Néel-type magnetic order in YbMnBi₂ [12]. Figure 1(a) demonstrates the presence of a spin-gap, $\Delta \gtrsim 10$ meV. The spin-wave dispersion bandwidth along $(H, 0, 0)$ is ≈ 50 meV,

which is similar to the values measured in CaMnBi₂ and SrMnBi₂ [13].

To uncover the coupling, we perform a quantitative analysis of the measured spectral function in the framework of a $J_1 - J_2 - J_c$ Heisenberg model (J_1, J_2 and J_c are the nearest and next-nearest neighbor in-plane and the inter-plane exchange interaction, respectively). In order to account for potential spin-wave damping, we use a damped-harmonic-oscillator (DHO) representation of the dynamical spin correlation function, $S(\mathbf{Q}, E)$,

$$S(\mathbf{q} + \mathbf{Q}_{\text{AFM}}, E) = S_{\text{eff}} \frac{1}{\pi} \frac{2(A_{\mathbf{q}} - B_{\mathbf{q}})}{1 - e^{-E/k_B T}} \times A \frac{\gamma E}{[E^2 - E_{\mathbf{q}}^2]^2 + (\gamma E)^2}. \quad (1)$$

Here, γ is the damping parameter (FWHM), k_B is the Boltzmann constant, S_{eff} is the effective fluctuating spin, and prefactor A ensures that the DHO spectral function is normalized to 1 (for $T, \gamma \rightarrow 0, A \rightarrow 1$) [24]. At $T \ll T_N$, spin wave theory gives $A_{\mathbf{q}} = 2S[2J_1 - 2J_2[\sin^2(\pi H) + \sin^2(\pi K)] - 2J_c \sin^2(\pi L) - D]$, $B_{\mathbf{q}} = 4S J_1 \cos(\pi H) \cos(\pi K)$, and $E_{\mathbf{q}}^2 = A_{\mathbf{q}}^2 - B_{\mathbf{q}}^2$.

We fit the data at each temperature using the cross-section given by Eq. (1) convolved with the instrumental resolution. The resulting fits are shown side-by-side with the data in Figures 1 and 2 (additional details provided in [24]). The best fit values thus obtained are shown in Table I. We find that the in-plane exchange parameters are nearly temperature-independent. The spin gap, Δ , which is determined by the effective uniaxial-anisotropy parameter, SD , decreases with increasing temperature and approaches zero above T_N .

Our crucial finding is a small and approximately \mathbf{Q} -independent damping parameter, γ , which is present at all temperatures. It increases by roughly a factor of 6 in the paramagnetic state, just above T_N , still remaining nearly \mathbf{Q} -independent. The \mathbf{Q} independence of γ is also supported by a supplementary analysis where energy (constant- \mathbf{Q}) cuts were fit with a DHO (Eq. (1), Eq. (S5) [24]) as illustrated in Fig. 3 (a)–(d). The static structure factor, $S(\mathbf{Q})$, and the correlation length, ξ , were also obtained in this procedure [24].

A comparison of γ to both the metallic/itinerant and local-moment magnetism scenarios unfolds the nature of spin-fermion interaction in YbMnBi₂. In itinerant antiferromagnets, such as iron and cobalt pnictide compounds, the signature of spin-fermion coupling in the magnetic excitation spectra is found in the form of anomalous broadening of spin waves due to their decay into particle-hole pairs. As a result, a large and anisotropic γ , increasing towards the zone boundary, is observed in the magnetically ordered state [21] and broad, diffusive-type spin fluctuations in the paramagnetic (PM) state [22, 23, 27, 28]. No such strong broadening in the antiferromagnetic state is seen in our

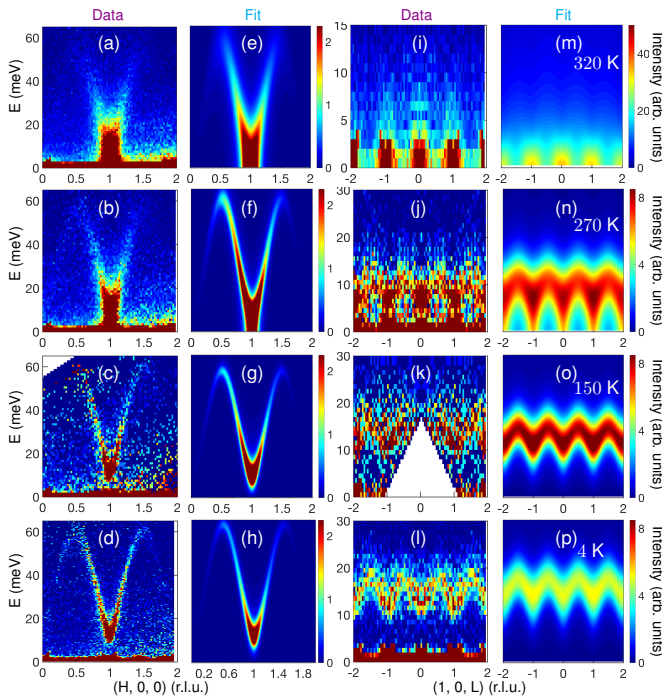


FIG. 2. INS spectra measured on YbMnBi₂ with $E_i = 100$ meV at $T = 320$ K, 270 K, 150 K and 4 K, illustrating the spin-wave dispersions along two symmetry directions, $(H, 0, 0)$ (a–d) and $(0, 0, L)$ (i–l). (e–h) and (m–p), INS spectra calculated using DHO, Eq. (1), for the same wave vectors as the data, using the results of fits given in Table I, and corrected for the instrument resolution (see [24] for details).

data, where γ is small and approximately \mathbf{Q} -independent [Table I, Fig. 3 (a)–(d)]. At the other extreme, there are no electronic excitations with which spin waves can interact in antiferromagnetic insulators. A comparison with relevant Mn-based compounds [14, 29] shows that the damping in these insulators is at least an order of magnitude smaller than what we find in YbMnBi₂.

We now calculate the correction to the spin susceptibility through coupling to the Dirac fermions within RPA and show that the observed damping is consistent with theoretical expectations for YbMnBi₂. The linear electronic dispersion in YbMnBi₂ predominantly arises from two-dimensional bands of Bi $6p$ states, which cross near the Fermi level [16]. If spin-orbit coupling and antiferromagnetism of YbMnBi₂ are neglected, the crossing is along an extended nodal line which originates in the staggered geometry of Yb with respect to the Bi square net [16, 30]. Although this nodal line reduces to a point upon inclusion of spin-orbit coupling and perfect antiferromagnetism of Mn atoms, four linear crossings (above the Fermi energy) are preserved in the Brillouin zone of YbMnBi₂ [16]. Importantly, as a “memory” of the nodal line, the resulting Fermi velocities are very anisotropic, with $v_{F\perp} \approx 9$ eVÅ perpendicular to the nodal line direction and $v_{F\parallel} \approx 0.043$ eVÅ along it [16, 17]. This extreme difference in the velocities will turn out to en-

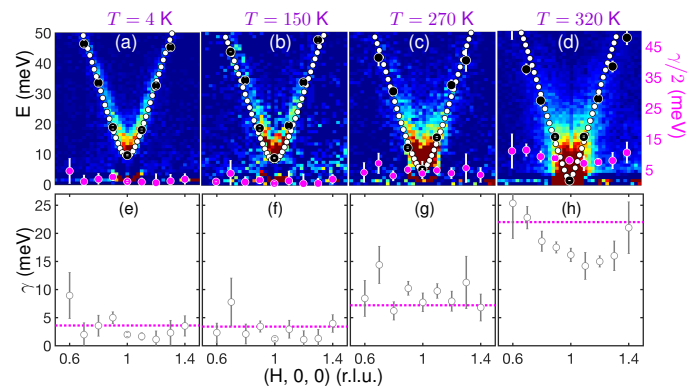


FIG. 3. \mathbf{Q} and temperature dependence of damping parameter, γ , and low-energy part of spin wave dispersion, $E_{\mathbf{q}}$. The under-damped spin wave exists where $E_{\mathbf{q}} > \gamma/2$. (a)–(d) \mathbf{Q} -independent damping parameter (magenta solid circles with white error bars showing one standard deviation) obtained from fitting 1D energy cuts using DHO response at $T = 4$ K, 150 K, 270 K and 320 K, respectively. Black circles show the corresponding spin wave energy, $E_{\mathbf{q}}$, which was fitted for all temperatures. White circles illustrate the dispersion obtained using the parameters in Table I for the corresponding temperature. (e)–(h) Open circles are fitted values from 1D data and magenta dashed lines are for 2D data given in Table I.

able low-energy scattering processes between spins and Dirac fermions that explain the observed damping.

We model the described system of spins and conduction electrons in YbMnBi₂ via the action,

$$\begin{aligned}
 S = & \int \frac{d^d p}{(2\pi)^d} \sum_{\eta=\pm} [\psi_{\eta}^{\dagger}(p) (ip_0 + \eta v_{1,\eta} \tau_x p_1 + v_{2,\eta} \tau_y p_2) \psi_{\eta}(p)] \\
 & + \frac{g}{2} \int \frac{d^d p}{(2\pi)^d} \int \frac{d^d q}{(2\pi)^d} [\mathbf{S}_{\mathbf{q}} \psi_{+}^{\dagger}(p) \boldsymbol{\sigma} \otimes \tau_x \psi_{-}(p-q) + \text{h.c.}] \\
 & + \int \frac{d^d q}{(2\pi)^d} \mathbf{S}_{\mathbf{q}} \chi_0^{-1} \mathbf{S}_{-\mathbf{q}}, \quad (2)
 \end{aligned}$$

which describes two Dirac cones at \mathbf{p}_{η} [$\eta = \pm$, see Fig. 4(a)] with anisotropic velocities, $v_{1,+} = v_{2,-} = v_{\perp}$ and $v_{1,-} = v_{2,+} = v_{\parallel}$, rotated with respect to each other ($v_{\parallel}/v_{\perp} \approx 0.005$ in YbMnBi₂). We use rotated coordinates, $p_{1,2} = (p_x \pm p_y)/\sqrt{2}$. Pauli matrices (τ) σ act on (pseudo-)spin, respectively. The Mn spin waves are represented by the three-component boson field, \mathbf{S} . Their dynamical susceptibility is given by the bare expression, without damping, $\chi_0^{-1}(E) = E^2 - E_{\mathbf{q}}^2$ [cf. Eq. (1)].

For simplicity, we perform calculations at $T = 0$ and in $d = 2 + 1$ dimensions. We assume that the Dirac points have opposite chirality, as was found in the related compound, SrMnBi₂ [30], and we consider a coupling, $\propto g$, which does not break chiral symmetry. In the coupling term in Eq. (2), we measure the wave vector transfer relative to the antiferromagnetic wave vector, $\mathbf{Q}_{\text{AFM}} = \mathbf{p}_{+} - \mathbf{p}_{-}$, which happens to connect the centers of the Dirac cones [see Fig. 4(a)]. Because of the

TABLE I. Exchange coupling, uniaxial anisotropy, and damping parameters for YbMnBi₂ obtained from fitting two-dimensional data shown in Fig. 2.

	$T = 4$ K	$T = 150$ K	$T = 270$ K	$T = 320$ K
SJ_1 (meV)	25.9 ± 0.2	24.4 ± 0.3	27.1 ± 0.5	25.6 ± 0.6
SJ_2/SJ_1	0.39 ± 0.01	0.40 ± 0.01	0.43 ± 0.01	0.41 ± 0.01
$ SJ_c /SJ_1$	0.0050 ± 0.0001	0.0041 ± 0.0001	0.0022 ± 0.0001	0.0016 ± 0.0001
SD (meV)	-0.20 ± 0.01	-0.16 ± 0.01	-0.06 ± 0.02	-0.003 ± 0.001
Δ (meV)	9.1 ± 0.2	8.0 ± 0.2	5.3 ± 0.8	1 ± 1
γ (meV)	3.6 ± 0.2	3.4 ± 0.2	7.2 ± 1.0	22.0 ± 4.0

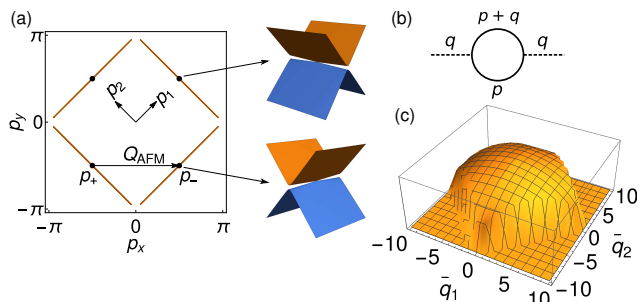


FIG. 4. (a) The Fermi surface resulting from the anisotropic Dirac cones and a shift of the crossing away from the Fermi surface. The Dirac cones are rotated with respect to each other as sketched to the right. The centers of the \mathbf{p}_+ and \mathbf{p}_- cones are connected by the antiferromagnetic wave vector $\mathbf{Q}_{AFM} = (\pi, 0)$. (b) Diagrammatic representation of the leading correction to the spin susceptibility through coupling to the Dirac electrons. Solid lines are Dirac propagators, dashed lines are spin waves. (c) The polarization $\text{Im}\Pi(E, \bar{q}_1, \bar{q}_2)$ obtained by numerical integration for an energy $E > \sqrt{2}v_{\parallel}q$ and $v_{\parallel}/v_{\perp} = 0.005$ as function of $\bar{q}_i = v_{\perp}q_i$.

large anisotropy, the elliptical Fermi surface is extremely elongated and appears very similar to a true nodal line.

The leading correction to the bare susceptibility due to coupling to the Dirac electrons renormalizes the spin susceptibility via the polarization, $\chi^{-1} = \chi_0^{-1} - \Pi$, Fig. 4(b). As the coupling is small and the semimetallic state in 2D Dirac materials is known to be stable due to a vanishing density of states at the Dirac points, we expect the second-order approximation for Π to adequately capture the damping effects,

$$\Pi(E, \mathbf{q}) = -\frac{g^2}{2} \int \frac{d^d p}{(2\pi)^d} \text{Tr}[G_+(p_0, \mathbf{p})\tau_x G_-(p_0 + E, \mathbf{p} + \mathbf{q})\tau_x], \quad (3)$$

with Dirac propagators, $G_{\eta}(p_0, \mathbf{p}) = (-ip_0 + \eta v_{1,\eta}\tau_x p_1 + v_{2,\eta}\tau_y p_2)/(p_0^2 + v_{1,\eta}^2 p_1^2 + v_{2,\eta}^2 p_2^2)$. The damping can be determined by the imaginary part of the retarded polarization after analytical continuation $ip_0 \rightarrow E + i0^+$. For general v_{\perp}, v_{\parallel} , we obtain a lengthy expression, which can be found in [24].

It is instructive to consider two limits. For isotropic

Dirac cones, $v_{\perp} = v_{\parallel} = v_F$, we find,

$$\text{Im}\Pi^R(E, \mathbf{q}) = \frac{N_f}{8v_F^2} g^2 \text{sign}(E) \sqrt{E^2 - v_F^2 \mathbf{q}^2} \Theta(E^2 - v_F^2 \mathbf{q}^2), \quad (4)$$

where N_f is the number of Dirac cone pairs and Θ is the step function. There are four Dirac points in each Brillouin zone of YbMnBi₂ [16, 17], so $N_f = 2$. Although Eq. (4) has approximately the correct functional form for the DHO ($\text{Im}\Pi^R \approx cE$), the kinematic constraint, $E > v_F|\mathbf{q}|$, usually cannot be satisfied because for most wave vectors electronic energies are much larger than the spin-wave energy. For $E^2 < v_F^2 \mathbf{q}^2$, the polarization function is purely real [31].

The extreme anisotropy of the electronic dispersion in YbMnBi₂ relaxes the kinematic constraint. For momentum transfers along \mathbf{Q}_{AFM} , corresponding to the data shown in Figs. 1–3, the leading order in small $(v_{\parallel}/v_{\perp})$ reads,

$$\text{Im}\Pi^R(E, q) \approx \frac{N_f}{2\pi v_{\perp}^2} g^2 E \Theta(E^2 - 2v_{\parallel}^2 q^2). \quad (5)$$

Accounting for further corrections leads to a weak momentum dependence [24]. The full numerical result for $\text{Im}\Pi^R$ is presented in Fig. 4. The main processes responsible for the enabled damping connect points along the elongated Fermi surfaces so that their energy cost is determined by v_{\parallel} . Due to its remarkable smallness, spin waves are able to excite such particle-hole pairs.

We conclude that the spin wave damping factor in Eq. (1) is given by $\gamma \approx N_f g^2 / (2\pi v_{\perp}^2)$. Thus, using $\gamma \approx 3.6$ meV (Table I), $N_f = 2$, $v_F = 9$ eV \AA , we can estimate the coupling constant, $g \approx 1.0$ eV $^{3/2}$ \AA . The obtained value of g quantifies the spin-fermion interaction in YbMnBi₂ and can be used, in future work, to analyze the effect of magnetism on the transport of Dirac electrons in the framework of Eq. (2).

In summary, we measured magnetic excitations in the Dirac material, YbMnBi₂, for temperatures in the range of $0.02 \leq T/T_N \leq 1.10$. The results show dispersing spin waves for all temperatures and their detailed analysis unfolds the nature of spin-fermion coupling between the

magnetic Mn layer and Dirac fermions of the Bi layer. We find a small, but distinct damping of spin waves, which for $T < T_N$ is weakly dependent on temperature and is nearly independent of wave vector. Despite its small magnitude, the observed damping indicates substantial spin-fermion coupling parameter, $g \approx 1.0 \text{ eV}^{3/2}\text{\AA}$, which we quantify by comparing the experiment with the theoretical analysis of model action for Dirac fermions coupled to spin waves, Eq. (2). Therefore, by combining the experimental measurements and theory, we establish the existence of long sought significant spin-fermion coupling in 112 family of Dirac materials.

We thank Alexei Tselvik and Michael Scherer for helpful comments and discussions. The work at Brookhaven was supported by the Office of Basic Energy Sciences, U.S. Department of Energy (DOE) under Contract No. DE-SC0012704. This research used resources at the Spallation Neutron Source, a DOE Office of Science User Facility operated by the Oak Ridge National Laboratory. LC acknowledges funding from a Feodor-Lynen research fellowship of the Humboldt foundation.

* sapkota@bnl.gov

† lclassen@bnl.gov

‡ Present address: School of Physics, Chongqing University, Chongqing 400044, China

§ zaliznyak@bnl.gov

- [1] T. Wehling, A. Black-Schaffer, and A. Balatsky, *Advances in Physics* **63**, 1 (2014).
- [2] M. Khodas, I. A. Zaliznyak, and D. E. Kharzeev, *Phys. Rev. B* **80**, 125428 (2009).
- [3] K. Wang, D. Graf, H. Lei, S. W. Tozer, and C. Petrovic, *Phys. Rev. B* **84**, 220401 (2011).
- [4] A. Wang, D. Graf, L. Wu, K. Wang, E. Bozin, Y. Zhu, and C. Petrovic, *Phys. Rev. B* **94**, 125118 (2016).
- [5] Y. Zhang, Y.-W. Tan, H.-L. Stormer, and P. Kim, *Nat.* **438**, 201 (2005).
- [6] M. Z. Hasan and C. L. Kane, *Rev. Mod. Phys.* **82**, 3045 (2010).
- [7] F. Katmis, V. Lauter, F. S. Nogueira, B. A. Assaf, M. E. Jamer, P. Wei, B. Satpati, J. W. Freeland, I. Eremin, D. Heiman, P. Jarillo-Herrero, and J. S. Moodera, *Nature* **533**, 513 (2016).
- [8] H. Masuda, H. Sakai, M. Tokunaga, Y. Yamasaki, A. Miyake, J. Shiogai, S. Nakamura, S. Awaji, A. Tsukazaki, H. Nakao, Y. Murakami, T.-h. Arima, Y. Tokura, and S. Ishiwata, *Sci. Adv.* **2** (2016), 10.1126/sciadv.1501117.
- [9] J. Park, G. Lee, F. Wolff-Fabris, Y. Y. Koh, M. J. Eom, Y. K. Kim, M. A. Farhan, Y. J. Jo, C. Kim, J. H. Shim, and J. S. Kim, *Phys. Rev. Lett.* **107**, 126402 (2011).
- [10] A. Zhang, C. Liu, C. Yi, G. Zhao, T.-l. Xia, J. Ji, Y. Shi, R. Yu, X. Wang, C. Chen, and Q. Zhang, *Nat. Commun.* **7**, 13833 (2016).
- [11] Y. F. Guo, A. J. Princep, X. Zhang, P. Manuel, D. Khalyavin, I. I. Mazin, Y. G. Shi, and A. T. Boothroyd, *Phys. Rev. B* **90**, 075120 (2014).
- [12] A. Wang, I. Zaliznyak, W. Ren, L. Wu, D. Graf, V. O. Garlea, J. B. Warren, E. Bozin, Y. Zhu, and C. Petrovic, *Phys. Rev. B* **94**, 165161 (2016).
- [13] M. C. Rahn, A. J. Princep, A. Piovano, J. Kulda, Y. F. Guo, Y. G. Shi, and A. T. Boothroyd, *Phys. Rev. B* **95**, 134405 (2017).
- [14] D. E. McNally, J. W. Simonson, J. J. Kistner-Morris, G. J. Smith, J. E. Hassinger, L. DeBeer-Schmitt, A. I. Kolesnikov, I. A. Zaliznyak, and M. C. Aronson, *Phys. Rev. B* **91**, 180407 (2015).
- [15] M. Chinotti, A. Pal, W. J. Ren, C. Petrovic, and L. Degiorgi, *Phys. Rev. B* **94**, 245101 (2016).
- [16] S. Borisenko, D. Evtushinsky, Q. Gibson, A. Yaresko, T. Kim, M. N. Ali, B. Buechner, M. Hoesch, and R. J. Cava, *arXiv:1507.04847* (2015).
- [17] D. Chaudhuri, B. Cheng, A. Yaresko, Q. D. Gibson, R. J. Cava, and N. P. Armitage, *Phys. Rev. B* **96**, 075151 (2017).
- [18] S. O. Diallo, V. P. Antropov, T. G. Perring, C. Broholm, J. J. Pulikkotil, N. Ni, S. L. Bud'ko, P. C. Canfield, A. Kreyssig, A. I. Goldman, and R. J. McQueeney, *Phys. Rev. Lett.* **102**, 187206 (2009).
- [19] R. J. McQueeney, S. O. Diallo, V. P. Antropov, G. D. Samolyuk, C. Broholm, N. Ni, S. Nandi, M. Yethiraj, J. L. Zarestky, J. J. Pulikkotil, A. Kreyssig, M. D. Lumsden, B. N. Harmon, P. C. Canfield, and A. I. Goldman, *Phys. Rev. Lett.* **101**, 227205 (2008).
- [20] D. C. Johnston, *Adv. Phys.* **59**, 803 (2010).
- [21] L. W. Harriger, H. Q. Luo, M. S. Liu, C. Frost, J. P. Hu, M. R. Norman, and P. Dai, *Phys. Rev. B* **84**, 054544 (2011).
- [22] A. Sapkota, B. G. Ueland, V. K. Anand, N. S. Sangeetha, D. L. Abernathy, M. B. Stone, J. L. Niedziela, D. C. Johnston, A. Kreyssig, A. I. Goldman, and R. J. McQueeney, *Phys. Rev. Lett.* **119**, 147201 (2017).
- [23] A. Sapkota, P. Das, A. E. Böhmer, B. G. Ueland, D. L. Abernathy, S. L. Bud'ko, P. C. Canfield, A. Kreyssig, A. I. Goldman, and R. J. McQueeney, *Phys. Rev. B* **97**, 174519 (2018).
- [24] See supplementary materials for additional details.
- [25] K. Wang, D. Graf, L. Wang, H. Lei, S. W. Tozer, and C. Petrovic, *Phys. Rev. B* **85**, 041101 (2012).
- [26] I. A. Zaliznyak, A. T. Savici, V. O. Garlea, B. Winn, U. Filges, J. Schneeloch, J. M. Tranquada, G. Gu, A. Wang, and C. Petrovic, *Journal of Physics: Conference Series* **862**, 012030 (2017).
- [27] S. O. Diallo, D. K. Pratt, R. M. Fernandes, W. Tian, J. L. Zarestky, M. Lumsden, T. G. Perring, C. L. Broholm, N. Ni, S. L. Bud'ko, P. C. Canfield, H.-F. Li, D. Vaknin, A. Kreyssig, A. I. Goldman, and R. J. McQueeney, *Phys. Rev. B* **81**, 214407 (2010).
- [28] W. Jayasekara, Y. Lee, A. Pandey, G. S. Tucker, A. Sapkota, J. Lamsal, S. Calder, D. L. Abernathy, J. L. Niedziela, B. N. Harmon, A. Kreyssig, D. Vaknin, D. C. Johnston, A. I. Goldman, and R. J. McQueeney, *Phys. Rev. Lett.* **111**, 157001 (2013).
- [29] S. P. Bayraki, D. A. Tennant, P. Leininger, T. Keller, M. C. R. Gibson, S. D. Wilson, R. J. Birgeneau, and B. Keimer, *Phys. Rev. Lett.* **111**, 017204 (2013).
- [30] G. Lee, M. A. Farhan, J. S. Kim, and J. H. Shim, *Phys. Rev. B* **87**, 245104 (2013).
- [31] J. González, F. Guinea, and M. A. H. Vozmediano, *Phys. Rev. Lett.* **77**, 3589 (1996).

SUPPLEMENTAL MATERIAL:

I. DAMPED HARMONIC OSCILLATOR STRUCTURE FACTOR FOR HEISENBERG SPIN MODEL

We analyzed the magnetic spectra using the $J_1 - J_2 - J_c$ Heisenberg model written as,

$$H = J_1 \sum_{\text{NN}} \mathbf{S}_i \cdot \mathbf{S}_j + J_2 \sum_{\text{NNN}} \mathbf{S}_i \cdot \mathbf{S}_j + J_c \sum_{\text{NN}(\perp)} \mathbf{S}_i \cdot \mathbf{S}_j + D \sum_i (S_i^z)^2 \quad (6)$$

Here, J_1 and J_2 are the in-plane nearest-neighbor (NN) and next-nearest-neighbor (NNN) antiferromagnetic (AFM) exchange interactions and J_c is the out-of-plane NN ferromagnetic (FM) interaction. The last term in Eq. (6) is the uniaxial anisotropy for the Mn spins corresponding to an easy axis along the c direction, which is quantified by the anisotropy parameter $D < 0$. Using the Holstein-Primakoff representation of spin operators, in harmonic approximation the following spin-wave dispersion relation is obtained [1, 2],

$$E_{\mathbf{q}} = \sqrt{A_{\mathbf{q}}^2 - B_{\mathbf{q}}^2}, \quad (7)$$

where $\mathbf{q} = \mathbf{Q} - \mathbf{Q}_{\text{AFM}} = (H, K, L)$ and,

$$A_{\mathbf{q}} = 4SJ_1 - 2SJ_2[2 - \cos(2\pi H) - \cos(2\pi K)] - 2SJ_c[1 - \cos(2\pi L)] - 2SD \\ = 4S[J_1 - J_2[\sin^2(\pi H) + \sin^2(\pi K)] - J_c \sin^2(\pi L) - D/2] \quad (8)$$

$$B_{\mathbf{q}} = 2SJ_1[\cos(\pi H + \pi K) + \cos(\pi H - \pi K)] = 4SJ \cos(\pi H) \cos(\pi K) \quad (9)$$

The magnetic neutron scattering cross-section for a system of spins can be written as [2-5],

$$\frac{d^2\sigma}{d\Omega dE} = Nr_m^2 \left| \frac{g}{2} F(\mathbf{Q}) \right|^2 \frac{k_f}{k_i} \sum_{\alpha, \beta} (\delta_{\alpha\beta} - \hat{Q}_\alpha \hat{Q}_\beta) S^{\alpha\beta}(\mathbf{Q}, E), \quad (10)$$

where N is the number of spins, $r_m = -5.39 \cdot 10^{-13}$ cm is magnetic scattering length, g is Lande spectroscopic g -factor, $F(\mathbf{Q})$ is the magnetic form factor (for YbMnBi₂, we use the magnetic form factor of Mn²⁺ ion with an adjustable covalent compression [6] p_{cov}), k_i and k_f are initial and final neutron wave vectors, respectively, and $S^{\alpha\beta}(\mathbf{Q}, E)$ is the dynamical structure factor describing spin-spin correlations. The dynamical structure factor is related to the imaginary part of dynamical spin susceptibility via the fluctuation-dissipation theorem,

$$S(\mathbf{Q}, E) = \frac{1}{\pi} \frac{\chi''(\mathbf{Q}, E)}{1 - e^{-E/k_B T}}. \quad (11)$$

The spectral function of a damped harmonic oscillator (DHO) accounts for the finite lifetime (non-zero inverse lifetime, $\Gamma = \gamma/2$) of a spin wave. The imaginary part of dynamical susceptibility for the DHO is [7],

$$\chi''(E) = \frac{\gamma E}{(E^2 - E_o^2)^2 + (\gamma E)^2}. \quad (12)$$

Here, $E_o = \hbar\omega_o$, where ω_o is the frequency of the oscillator. To meet the requirement of the sum rule for the spin dynamical structure factor [4], normalization of the DHO spectral function of Eq. (11) has been implemented by calculating a prefactor, $A^{-1} = \int_{-\infty}^{\infty} S(\mathbf{Q}, E) dE$, at each \mathbf{Q} . Using this normalization of $S(\mathbf{Q}, E)$ with respect to energy and Eqs. (11) and (12), we obtain the dynamical structure factor for spin waves at $T \ll T_N$,

$$S(\mathbf{q} + \mathbf{Q}_{\text{Néel}}, E) = S_{\text{eff}} \frac{1}{\pi} \frac{2(A_{\mathbf{q}} - B_{\mathbf{q}})}{1 - e^{-E/k_B T}} \\ \times A \frac{\gamma E}{[E^2 - E_{\mathbf{q}}^2]^2 + (\gamma E)^2}, \quad (13)$$

where k_B is the Boltzmann constant, γ is the damping parameter corresponding to Lorentzian full width at half maximum (FWHM), and S_{eff} is the effective fluctuating spin. In the limit of $\gamma \rightarrow 0$ and for $S_{\text{eff}} = S$ it corresponds to the delta function contributions describing an undamped linear spin wave [3].

II. SPIN WAVE DISPERSION FROM ONE-DIMENSIONAL ENERGY CUTS

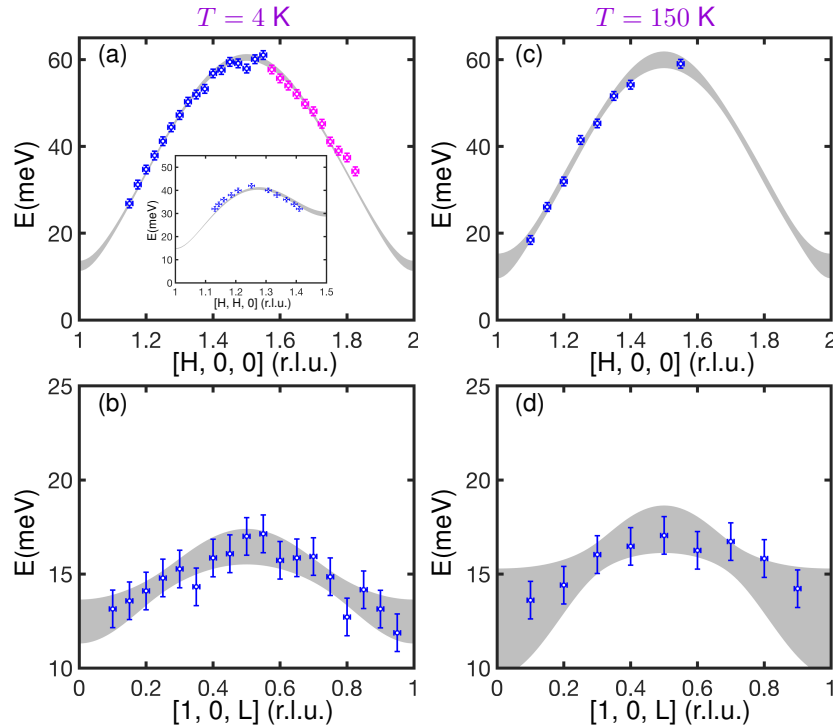


FIG. S1. Spin-wave dispersions along high-symmetry directions, $(H, 0, 0)$ and $(1, 0, L)$, for 4 K (a, b) and 150 K (c, d). The grey-shaded region represents the 95% confidence interval of the fitting results given in Table II. In (a), blue and magenta circles are obtained from two different E vs $(H, 0, 0)$ dispersion data. Blue is from the data in which only $L = \text{integers}$ are averaged while the whole range of $L = -6$ to 6 were averaged for magenta. Only the blue data were used for the fit. The inset shows dispersion along the $(H, H, 0)$ direction. Error bars represent one standard deviation.

One-dimensional dispersion data along $(H, 0, 0)$ and $(1, 0, L)$ directions at temperatures 4 K and 150 K shown in Fig. S1 were obtained using the peak position of one-dimensional (constant- \mathbf{Q}) energy cuts of the two-dimensional (2D) magnetic scattering spectra shown in Fig. 3 of the main text. These 1D energy cuts were fitted using the Gaussian lineshape and accounting for Gaussian instrumental energy resolution. We note that this procedure does not account for the additional width, as well as the shift of the peak position measured near the bottom (top) of dispersion to higher (lower) energy, resulting from the convolution of spin wave dispersion with the wave vector resolution.

The peak positions thus obtained were used to create the dispersion plots shown in Fig. S1, which are consistent with 2D plots of Fig. 3 of the main text. The results obtained by fitting these 1D data with spin wave dispersion relation given by Eqs. (7)–(8) are shown in Table II. They are fairly close to the results obtained from 2D fits presented in Table I of the main text. The underestimate of J_1 and overestimate of Δ in Table II result from the wave vector resolution effect mentioned above, thus providing an estimate of the magnitude of this effect. The wave vector resolution is properly accounted for, in the analysis presented in the main text, as described below.

III. FITTING PROCEDURE

Prior to fitting the 2D data shown in the main text, we first fit 1D dispersions for $T = 4$ K and 150 K shown in Fig. S1. The fit parameters thus obtained (Table II) are used as initial values for the fits of the 2D intensities shown in Fig. 3 of the main text. For higher temperatures, 270 K and 320 K, the values obtained from the fit of 2D data at $T = 4$ K are used for initial parameters.

For 4 K and 150 K, the data sets corresponding to the dispersions along $(H, 0, 0)$ and $(1, 0, L)$ directions were fitted simultaneously. For 270 K data, the in-plane exchange and the anisotropy parameters were first obtained by fitting the data along $(H, 0, 0)$ direction and then these parameters were fixed to the fitted values and J_c was obtained from

TABLE II. Exchange and uniaxial anisotropy parameters and spin gap for YbMnBi₂ obtained from fitting of the one-dimensional dispersion plots at $T = 4$ K and 150 K shown in Fig. S1.

	$T = 4$ K	$T = 150$ K
SJ_1 (meV)	22.70 ± 0.28	23.76 ± 1.16
SJ_2 (meV)	7.79 ± 0.20	8.77 ± 1.01
SJ_c (meV)	-0.16 ± 0.03	-0.19 ± 0.06
SD (meV)	-0.43 ± 0.04	-0.41 ± 0.07
Δ (meV)	12.44 ± 0.9	12.42 ± 1.16

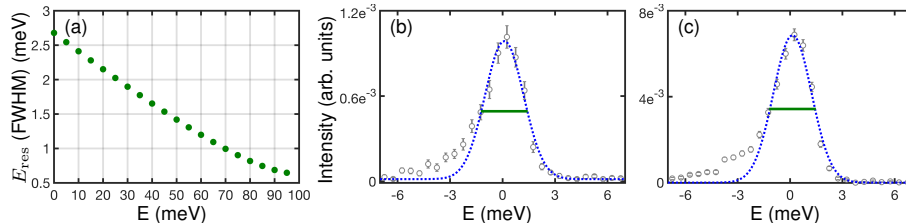


FIG. S2. (a) Energy resolution FWHM vs energy transfer for the incident energy $E_i = 100$ meV and high-resolution SEQUOIA Fermi chopper spinning at 600 Hz, corresponding to our measurement configuration. The E_{res} are calculated using the methods discussed in Refs. 8, 9. (b) and (c) E -cuts at $(0.45, 0, 0)$ and $(1.45, 0, 0)$, respectively, through $E = 0$ meV showing incoherent peaks. Cuts are taken from the data measured at $T = 4$ K. Blue dotted lines are fits to a Gaussian lineshape using only $E > -2$ meV data and green solid lines represent the instrumental resolution width for $E = 0$ meV shown in panel (a).

the simultaneous fit of $(1, 0, L)$ and $(H, 0, 0)$ data. For all the different fit procedures that we tried for 270 K data, the fitted values of $\Gamma = \gamma/2$ were in the range 2.5 – 4.8 meV and the average value is reported as the best fit parameter in the main text. For 300 K, the paramagnon is overdamped near $(1, 0, 0)$ for $E < \Gamma$ and $(1, 0, L)$ dispersion is not defined. Hence, the simultaneous fitting produces insensible imaginary results. We therefore obtained the values of the in-plane exchange, anisotropy, and damping parameters by fitting the data along $(H, 0, 0)$ for $E > \Gamma$ and then estimated J_c from the L -dependent response of an over-damped oscillator by fitting the data along $(0, 0, L)$ with these parameters fixed. All the fits were carried out with the magnetic form factor of Mn^{2+} , but using an adjustable covalent compression p_{cov} , $F(Q) = F_{\text{Mn}^{2+}}(p_{\text{cov}}Q)$, similar to Ref. 6. The covalent compression was fitted for 4 K data and was kept fixed to the refined value, $p_{\text{cov}} = 1.49(4)$, for data at higher temperatures.

A. Account for the energy resolution

The fits were carried out using the DHO cross-section given by Eqs. (10)–(12) convolved with a Gaussian lineshape in energy representing the instrumental energy resolution. In order to avoid the contamination of the inelastic signal by the incoherent elastic background and magnetic Bragg peaks, only the data at $E > 7$ meV for $T = 4$ K and 150 K and at $E > 5$ meV for $T = 270$ K and 320 K were used for fitting.

The FWHM of the Gaussian energy resolution, E_{res} , was calculated using the method discussed in Refs. 8, 9. Fig. S2 presents E_{res} calculated for the high-resolution configuration with $E_i = 100$ meV and SEQUOIA narrow-slotted Fermi-chopper #2 spinning at 600 Hz used in our measurements. These values were used in convolution with the calculated cross-section for fitting the data. Fig. S2 (b) and (c) illustrate that the calculated resolution at $E = 0$ meV very accurately reproduces the width of exemplary incoherent elastic scattering peaks at wave vectors $(0.45, 0, 0)$ and $(1.45, 0, 0)$, respectively. This indicates that instrumental energy resolution is accurately accounted for in our analysis and the widths given in Table I of the main text represent the intrinsic broadening of the spin wave peaks.

B. Account for the wave vector resolution

As shown in Sec. A above, the energy resolution used in our high-resolution measurements is smaller than the intrinsic physical width of the spin wave peak extracted from our fits, which we assign to spin wave damping via

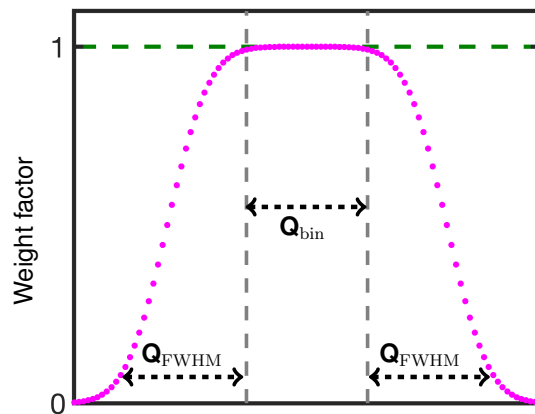


FIG. S3. Illustration of the wave vector line shape used in our fits to account for the \mathbf{Q} resolution. \mathbf{Q}_{bin} is the range of the actual data bin used to create our plots and \mathbf{Q}_{FWHM} is the calculated value of Q resolution, using the methods discussed in Ref. 8. In our fits of 2D data, the spin wave intensity at each \mathbf{Q} was obtained as a sum of intensities within the window of size $\mathbf{Q}_{\text{bin}} + 2\mathbf{Q}_{\text{FWHM}}$ weighted by the resolution weight function shown in the figure and normalized to 1, both centered at this \mathbf{Q} .

decays into Dirac electron-hole pairs. The overall resolution correction to the width of the spin wave peak is also sensitive to the effect of wave vector resolution. The FWHM of the instrumental \mathbf{Q} resolution was similarly calculated using the equations given in Ref. 8 and accounting for the sample mosaic of 0.8° . The average value of \mathbf{Q}_{FWHM} in the 5 meV energy transfer window was used in our fits.

In order to account for the additional wave vector broadening due to the binning of the data at each \mathbf{Q} , the Gaussian wave vector resolution was convoluted with the window function corresponding to the wave vector range used for binning. This results in a \mathbf{Q} resolution function in the form of two complementary error functions parameterized by the \mathbf{Q} -resolution FWHM, \mathbf{Q}_{FWHM} , and the bin size, \mathbf{Q}_{bin} , as shown in Fig. S3. In order to minimize the effect of wave vector resolution and still have sufficient intensity for reliable fitting, we used the optimized bin size of ± 0.0125 and ± 0.05 along $(H, 0, 0)$ and $(0, K, 0)$, respectively, for all the $E_i = 100$ meV and $E_i = 35$ meV data, except for 320 K data, for which ± 0.1 along $(0, K, 0)$ direction was used; the bin size in $(0, 0, L)$ was kept at ± 0.1 .

C. The manifestation of the intrinsic physical width in the line shape of spin wave peak

Figures S4 (a)–(f) present the best fits of the one-dimensional energy cuts of the 4 K data with and without account for intrinsic spin wave peak width, γ , which demonstrate the effect of non-negligible broadening on the measured spin waves. Green dotted lines are fits with $\gamma = 2\Gamma = 0.02$ meV and blue lines are fits with free γ . The χ^2 corresponding to the green lines with negligible damping is systematically larger than that of blue lines where γ was fit. Green lines are also clearly less accurate in describing the broad tail of the spin wave peak, which is especially apparent in panels (c) – (f). The difference is clear, indicating that intrinsic width, $\gamma \gtrsim 2$ meV, is indeed present even at the lowest temperature.

IV. TEMPERATURE DEPENDENCE OF THE DYNAMICAL CORRELATION LENGTH

Figure S5, (a)–(d), illustrates the \mathbf{Q} variation of $\gamma/2 = \Gamma$. The values are obtained by fitting the 1D energy cuts with DHO, Eq. (13). The data in the panels are the same as in Fig. 3 of the main text and corroborate the \mathbf{Q} -independence of Γ for all temperatures, consistent with our fits of 2D data shown in the main text. The fits also provide the static structure factor, $S(\mathbf{Q})$, which is shown in Fig. S5 (e)–(h). By fitting $S(\mathbf{Q})$ to a lattice Lorentzian [4, 10], we obtain the correlation length for spin fluctuations, ξ . Fig. S5 (i) illustrates the temperature dependence of thus obtained correlation length, which, as expected, increases on approaching the transition temperature, T_N , indicating critical phenomena.

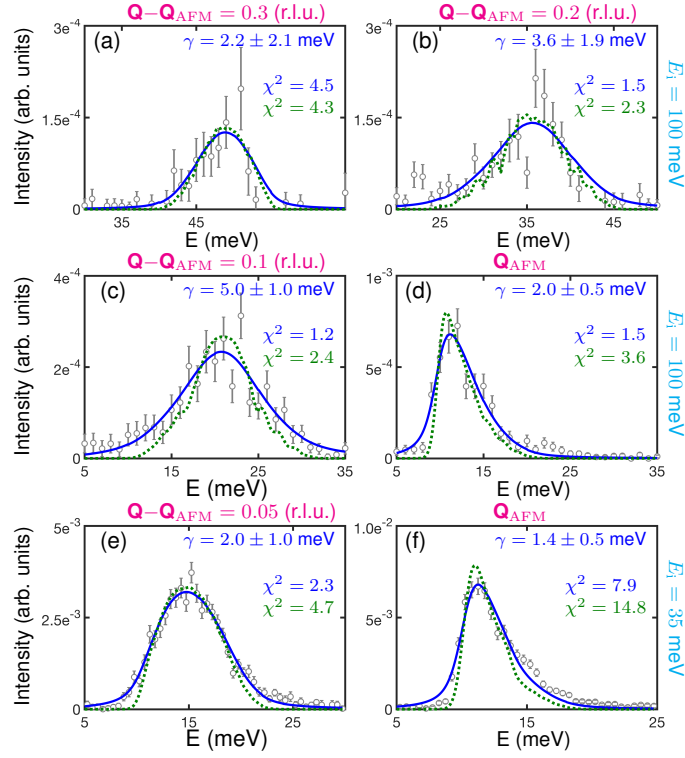


FIG. S4. Selected one-dimensional E -cuts of $T = 4$ K data with resolution-corrected fits to Eq. (13). (a)–(d) cuts at four \mathbf{Q} points along the $(H, 0, 0)$ direction for the data measured with $E_i = 100$ meV. (e) and (f) cuts at two \mathbf{Q} points near the bottom of the dispersion for the data measured with $E_i = 35$ meV. Blue solid lines are the DHO fits, Eq. (13), where γ was varied and green dotted lines are fits with fixed $\gamma = 0.02$ meV. Fitted values of γ obtained for the blue lines are given in each figure. Data are averaged over the range of ± 0.0125 and ± 0.05 along $(H, 0, 0)$ and $(0, K, 0)$, respectively. Error bars in all figures represent one standard deviation.

V. TEMPERATURE DEPENDENCE OF THE SPIN GAP

In addition to the spin gap obtained from fitting the 2D dispersion discussed above and in the main text, the spin gap at a number of temperatures was measured in a set of limited rotation scans on HYSPEC at SNS, ORNL. The measurements were carried out with incident energy of $E_i = 30$ meV and by rotating the sample about its vertical axis in 1° steps over $\approx 60^\circ$ range. The results are shown in Fig. S6. To obtain the values of spin gap, the energy cuts shown in Fig. S6 (a) are fitted with the gap equation given in Ref. 1. Fig. S6 (b) illustrates the temperature dependence of the spin gap and shows that the spin gap follows the order parameter temperature dependence and vanishes at $T \approx T_N$, as expected for a spin wave [11].

VI. GENERAL EXPRESSION OF POLARIZATION BUBBLE

With the coupling between Dirac electrons and spin as given in the main text, we obtain within RPA for the polarization

$$\text{Im}\Pi^R(E, \mathbf{q}) = -\frac{N_f}{4\pi v_\perp^2} g^2 \text{sign}(E) \int_0^1 dx \Theta \left(E^2 - \alpha^2 \left(\frac{\bar{q}_1^2}{1-x+\alpha^2 x} + \frac{\bar{q}_2^2}{x+\alpha^2(1-x)} \right) \right) \frac{1}{\sqrt{(1-x+\alpha^2 x)(x+\alpha^2(1-x))}} \times \left[-\sqrt{|\Delta_2|} + \frac{\Delta_1}{\sqrt{|\Delta_2|}} - \alpha \frac{1+\alpha^2}{(1-x+\alpha^2 x)(x+\alpha^2(1-x))} \sqrt{|\Delta_2|} \right] \quad (14)$$

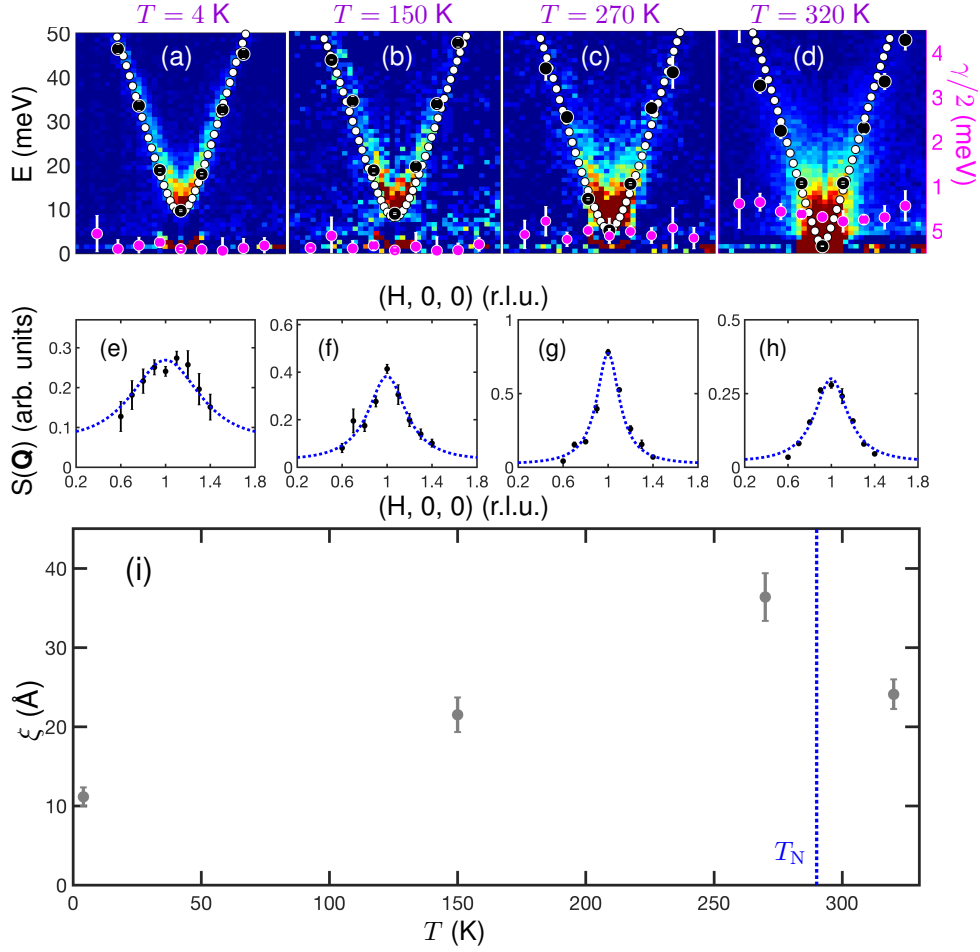


FIG. S5. \mathbf{Q} and temperature dependence of the damping parameter, $\gamma/2 = \Gamma$, and the correlation length, ξ , respectively. The under-damped spin wave exists where $E_{\mathbf{q}} > \Gamma$. (a)–(d) \mathbf{Q} -independent damping parameter (magenta solid circles with white error bars) obtained from fitting 1D energy cuts using DHO response at $T = 4$ K, 150 K, 270 K and 320 K, respectively. Black circles show the corresponding spin wave energy, $E_{\mathbf{q}}$, which was fitted for all temperatures. White circles illustrate the dispersion obtained using the parameters in Table I of the main text for the corresponding temperature. (e)–(h) $S(\mathbf{Q})$ obtained from the fits of 1-D energy cuts using DHO. The blue dotted lines are fits using the 1D lattice Lorentzian function [4, 10]. (i) Temperature dependence of the correlation length. Error bars in all figures represent one standard deviation.

with

$$\Delta_2 = x(1-x) \left[-E^2 + \alpha^2 \left(\frac{\bar{q}_1^2}{1-x + \alpha^2 x} + \frac{\bar{q}_2^2}{x + \alpha^2(1-x)} \right) \right] \quad (15)$$

$$\Delta_1 = x(1-x) \left[-E^2 + \alpha^3 \left(\frac{\bar{q}_1^2}{(1-x + \alpha^2 x)^2} + \frac{\bar{q}_2^2}{(x + \alpha^2(1-x))^2} \right) \right] \quad (16)$$

and $\alpha = v_{\parallel}/v_{\perp}$, $\bar{q}_i = v_1 q_i$, i.e. $\alpha \bar{q}_i = v_{\parallel} q_i$. We also introduced a Feynman parameter, x . Expanding in small α , we see that in this case the kinematic constraint is indeed relaxed, giving the expected damping. Let us consider momentum transfers along the antiferromagnetic wave vector, which corresponds to $q_1 = q_2 = q/\sqrt{2}$. The leading order then reads,

$$\text{Im}\Pi^R(E, q) \approx \frac{N_f}{2\pi v_{\perp}^2} g^2 E \Theta(E^2 - 2v_{\parallel}^2 q^2), \quad (17)$$

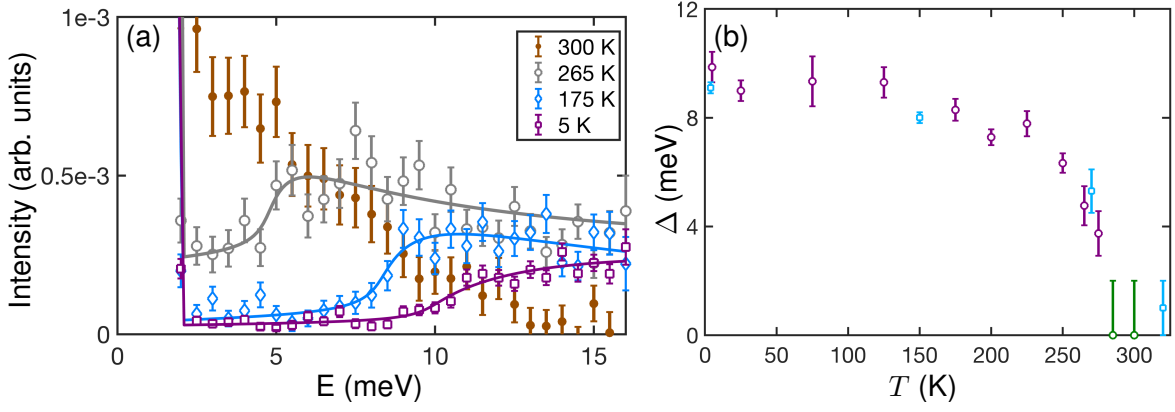


FIG. S6. (a) One-dimensional E -cuts at $(1,0,1)$ at 4 different temperature for the HYSPEC data measured with incident energy $E_i = 30$ meV. Solid lines are fits to the data using the gap equation in Ref. 1 and a Gaussian lineshape for the peak at zero energy. Figure illustrates that increase in intensity, at ≈ 8.5 meV for $T = 5$ K, which represents the gap energy, shifts to lower energy with increasing temperature. The gap feature is not discernible for 300 K data. (b) Temperature dependence of the gap. Open circles are from the HYSPEC data and blue squares are from the fits of the SEQUOIA data listed in Table I of the main text. Fits are discussed in the Section V. For 285 and 300 K, where gaps are no more discernible, gap is fixed at 0 with error of 2 meV, which is approximately the full width at half maximum of elastic zero-energy peak.

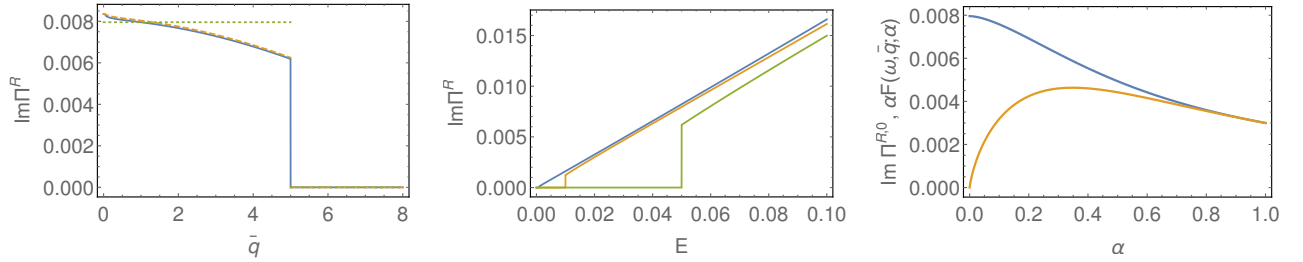


FIG. S7. (left) Polarization as function of momentum transfer for fixed energy $E = 50$ meV and anisotropy $\alpha = 0.005$. We show different approximations: full numerical expression, Eq. (14), (solid), expansion in α with corrections, Eq. (18), (dashed), and only the leading term, Eq. (17), which is momentum-independent (dotted). The kinematic constraint, i.e. the location where the damping vanishes, is well reproduced in all cases. (middle) Polarization as function of energy for different momentum transfers, $v_\perp q = 0.1, 1$, and 5 eV. For energies that are larger than the threshold required to excite a particle-hole pair, $E > v_\parallel q$, the polarization for a fixed momentum is a linear function of energy, as described by Eq. (17). The vertical displacement can be estimated as $\frac{N_f}{8\pi v_\perp^2} g^2 \alpha F(0, q)$ with $\alpha F(0, q) \approx 4\alpha\bar{q}$. (right) Numerically calculated $\alpha F(\omega, \bar{q}, \alpha)$ (orange) and leading contribution to the polarization, $\text{Im}\Pi^{R,0} = \text{Im}\Pi^R - \alpha F$ (blue), as function of α for $\omega = 50$ meV and $\bar{q} = 10$ meV. For the experimental value of α in YbMnBi_2 , $\alpha \approx 0.005$, the correction is negligible.

as given in the main text. Accounting for small corrections, we find,

$$\text{Im}\Pi^R(\omega, \bar{q}) \approx -\frac{N_f}{4\pi v_\perp^2} g^2 \text{sign}(\omega) \Theta(\omega^2 - 2\alpha^2 \bar{q}^2) \left[-2\omega E \left(1 - \frac{2\alpha\bar{q}^2}{\omega^2} \right) + \frac{2\alpha^2 \bar{q}^2}{\omega^2} K \left(1 - \frac{2\alpha\bar{q}^2}{\omega^2} \right) \right] + \frac{N_f}{8\pi v_\perp^2} g^2 \alpha F(\omega, q; \alpha), \quad (18)$$

where $K(x)$ and $E(x)$ are the complete elliptic functions of first and second kind, and

$$F(\omega, \bar{q}; \alpha) = -\int_0^1 dx \Theta(\omega^2 x(1-x) - \alpha^2 \bar{q}^2/2) \frac{1 + \alpha^2}{\sqrt{(1-x + \alpha^2 x)(x + \alpha^2(1-x))}^3} \sqrt{|\omega^2 x(1-x) - \alpha^2 \bar{q}^2/2|}. \quad (19)$$

Although the integration and the limit $\alpha \rightarrow 0$ in $\alpha F(\omega, q; \alpha)$ do not commute, for zero momentum transfer we find $\alpha F(\omega, \bar{q} = 0) \approx 4\omega\alpha \log \alpha$ and in the static limit, $\alpha F(\omega = 0) \approx 4\alpha\bar{q}$. We present the numerical result $\alpha F(\omega, \bar{q})$ and compare the different approximations in Fig S7.

* sapkota@bnl.gov

† lclassen@bnl.gov

‡ Present address: School of Physics, Chongqing University, Chongqing 400044, China

§ zaliznyak@bnl.gov

- [1] M. Ramazanoglu, A. Sapkota, A. Pandey, J. Lamsal, D. L. Abernathy, J. L. Niedziela, M. B. Stone, A. Kreyssig, A. I. Goldman, D. C. Johnston, and R. J. McQueeney, *Phys. Rev. B* **95**, 224401 (2017).
- [2] M. C. Rahn, A. J. Princep, A. Piovano, J. Kulda, Y. F. Guo, Y. G. Shi, and A. T. Boothroyd, *Phys. Rev. B* **95**, 134405 (2017).
- [3] G. L. Squires, *Introduction to the Theory of Thermal Neutron Scattering*, 2012th ed. (Cambridge University Press, England, 1978).
- [4] I. A. Zaliznyak and S.-H. Lee, in *Modern Techniques for Characterizing Magnetic Materials*, edited by Y. Zhu (Springer US, 2005) pp. 3–64.
- [5] A. Sapkota, B. G. Ueland, V. K. Anand, N. S. Sangeetha, D. L. Abernathy, M. B. Stone, J. L. Niedziela, D. C. Johnston, A. Kreyssig, A. I. Goldman, and R. J. McQueeney, *Phys. Rev. Lett.* **119**, 147201 (2017).
- [6] I. Zaliznyak, A. T. Savici, M. Lumsden, A. Tselik, R. Hu, and C. Petrovic, *Proc. Natl. Acad. Sci.* **112**, 10316 (2015).
- [7] J. Lamsal and W. Montfrooij, *Phys. Rev. B* **93**, 214513 (2016).
- [8] G. Ehlers, A. A. Podlesnyak, J. L. Niedziela, E. B. Iverson, and P. E. Sokol, *Rev. Sci. Instrum.* **82**, 085108 (2011).
- [9] D. L. Abernathy, M. B. Stone, M. J. Loguillo, M. S. Lucas, O. Delaire, X. Tang, J. Y. Y. Lin, and B. Fultz, *Rev. Sci. Instrum.* **83**, 015114 (2012).
- [10] A. T. Savici, I. A. Zaliznyak, G. D. Gu, and R. Erwin, *Phys. Rev. B* **75**, 184443 (2007).
- [11] E. G. Sergeicheva, S. S. Sosin, L. A. Prozorova, G. D. Gu, and I. A. Zaliznyak, *Phys. Rev. B* **95**, 020411 (2017).